Topological massive Dirac fermions in β-tungsten

Jiangxu Li,[1,2] Sami Ullah,[1,3] Ronghan Li,[1,2] Mingfeng Liu,[1,2] Hongtao Cao,[4] Dianzhong Li,[1] Yiyi Li,[1] and Xing-Qiu Chen[1,*]

[1]*Shenyang National Laboratory for Materials Science, Institute of Metal Research, Chinese Academy of Sciences, Shenyang 110016, China*

[2]*School of Materials Science and Engineering, University of Science and Technology of China, 110016 Shenyang, Liaoning, China*

[3]*University of Chinese Academy of Sciences, Beijing 100049, China*

[4]*Ningbo Institute of Materials Technology and Engineering, Chinese Academy of Sciences, Ningbo 315201, China*

(Received 25 September 2018; published 8 April 2019)

Ultrathin films of β-tungsten (β-W) is attracting extensive attentions because of its promising application in spintronics due to giant spin Hall effect and its fundamental interest in superconductivity. By means of first-principles calculations, we have elucidated its nontrivial topological nature with multiple Dirac nodal lines in the β-W metal when spin-orbit coupling (SOC) is ignored. The analysis of electronic structures reveal that its topology is associated with the band inversion between the $d_{xz} + d_{yz}$ and d_{z^2} orbitals at the M point in its Brillouin zone. By switching on the SOC, these Dirac nodal lines become gapped, as accompanied with the occurrence of 24 massive Dirac fermions at the energy of 87 meV below the Fermi level. Different from the exact gapless Dirac fermions with the linear band crossings, we have identified that these massive Dirac fermions all open a tiny gap of 7 meV. In addition, we have observed the topologically protected nontrivial surface arc states connecting these massive Dirac fermions. The existence of these massive Dirac fermions in the β-W phase would be important to understand its giant spin Hall effect according to a recent study [Nature **555**, 638 (2018)] where massive Dirac fermions were identified to generate Berry-curvature-induced Hall conductivity.

DOI: 10.1103/PhysRevB.99.165110

I. INTRODUCTION

Tungsten usually crystalizes in the ground-state α A2 (body-centered cubic) crystal structure (bcc, space group $Im\bar{3}m$) [1–4] or in the metastable β (A15 usually in thin films) [3,4] structure with the versatile and intriguing properties of high thermal conductivity, low sputtering erosion, very high melting point (3695 K), strong mechanical resistance and high hardness, and excellent thermal/chemical stabilities, as well as distinctive electrical and optical properties. Beside its important applications in structured materials and potential candidates for plasma-facing components for future fusion reactors [5], recently tungsten has attracted great attention for applications in both microelectronics and spintronics. For instance, α-W films are highly desirable for interconnects or diffusion barriers in integrated circuits, whereas β-W films generally have superior catalytic activity and high spin-orbit coupling for magnetic memory applications [6]. Typically, W films or nanowires with preferred orientations are utilized as interconnects in microelectronics. Tungsten has severed as a potential replacement for Cu in semiconductor metallization because its shorter electron mean free path of 19.1 nm can offer the possibility of a lower resistance than Cu at reduced line dimensions [3,7]. Photonic crystals consisting of tungsten nanoparticle stacks or W/HfO_2 alternative structures were applied to harvest solar energy [8]. W films could also be served as functional layers in thermionic energy converters. The resistivity of α-W films ($\sim$20 $\mu\Omega$ cm) is significantly lower than that of the β-W counterparts ($\sim$150 $\mu\Omega$ cm) [9–11].

In particular, it needs to be emphasized that the ultrathin film of β-tungsten has its promising potentials for spintronic applications [12], which usually make use of both spin and charge degrees of freedom to control the transport properties of materials and devices. One of the key aspects of spintronics is to explore how to efficiently manipulate the magnetization of a ferromagnet. There are two ways to realize the magnetization manipulation. One is to control the magnetic field and the other one is to use the spin transfer torque generated by the spin-polarized current, which is originated from the spin Hall effect (SHE). Due to the large spin-orbit coupling in heavy elemental solids, Pt [13,14], Ta [15], and W [10,11,16] are materials among the nonmagnetic transition metals with large SHE. Importantly, the highly resistive metastable β-W phase ($\rho_{\beta\text{-W}} \sim$ 100–300 $\mu\Omega$ cm) was reported to exhibit a giant spin Hall effect with a spin Hall angle, $\theta_{SH} \sim -0.3$ to -0.4 [10,11,16], defined by the ratio of the spin Hall conductivity to the diagonal charge conductivity due to the strong spin-orbit coupling (SOC) effect. To date, the β-W has been known to exhibit the largest spin Hall angle among all known elemental transition metal solids. Hence, β-W potentially provides an efficient way of manipulating the magnetization, because of its large spin Hall angle for the current-driven spin-orbit torques in heavy metal/ferromagnetic heterostructures. Recently, the underlying mechanism of the intrinsic spin Hall conductivity of β-W was theoretically revealed to be the cooperative behavior of the giant spin Hall conductivity and a much smaller longitudinal conductivity in its bulk phase [11]. Surprisingly, the topological insulator Bi_2Se_3 was most recently proposed and experimentally exhibit the large

*Corresponding author: xingqiu.chen@imr.ac.cn

spin-orbit torques and the extremely large θ_{SH} as high as 2.0–3.5 [17] because of its helical spin-polarized nontrivial topological surface states. These unique facts mentioned here have inspired us to check back the electronic structures of β-tungsten.

Within this context, through first-principles calculations we have revisited the electronic structures of β-tungsten. We have identified that β-tungsten is a topological massive Dirac metal. When the SOC is neglected, DNLs exist in its BZ and their existences are indeed associated with the band inversion between $d_{xz}+d_{yz}$ and d_{z^2} orbitals at the high-symmetry M point. Once the SOC is switched on, there only exist 24 massive Dirac fermions (MDFs) [18,19]. Furthermore, the nontrivial topologically protected surface states and Fermi arcs also have been obtained. Our work proposes a pure topological massive Dirac metal of β-tungsten and paves the way for more experimental studies on its electronic and transport properties.

II. METHODS

The first-principles calculations within the framework of density functional theory (DFT) [20,21] have been performed to investigate the electronic and phonon structures by employing the Vienna *ab initio* simulation package (VASP) [22,23]. We employed the projector-augmented-wave (PAW) [24] pseudopotentials and Perdew-Burke-Ernzerhof (PBE) exchange and correlation functionals [25]. A self-consistent field method (tolerance 10^{-6} eV/atom) is employed in conjunction with plane-wave basis sets of a cutoff energy of 500 eV, while a M center Monkhorst-Pack grid of $15\times15\times15$ is used for the BZ integrals. For the lattice constants optimization, the remanent Hellmann-Feynman forces are less than 0.0001 eV/Å. The force constants are obtained by using the density functional perturbation theory method [26] implemented in the Phonopy [27] within a Born-Karman boundary condition in a supercell containing $3\times3\times3$ primitive cells. The maximally localized Wannier functions from the first-principles calculations have been constructed for the tight-binding model. The projected surface states are obtained from the surface Green's function [28] of the semi-infinite system to check its nontrivial surface states.

III. RESULTS AND DISCUSSIONS

A. Structure

β-W crystalizes in a closed-packed A15 structure with a space group of $Pm\bar{3}n$ (No. 223), as shown in Fig. 1(a). Its unit cell structure is composed of four atomic layers paralleling to the (100) plane, in which two W atoms locate at the 2b Wyckoff site and six W atoms occupy the 6a Wyckoff sites. Our first-principles calculations yielded that the optimized lattice constant $a=5.06$ Å is in good agreement with previous experimental [29,30] and calculated results [4]. The derived phonon dispersion [Fig. 1(c)] does not show any imaginary part of the frequency and it is dynamically stable. Figure 1(b) shows the first Brillouin zone (BZ), in which the gray plane is a mirror plane and the projected (001) surface BZ zone has been sketched.

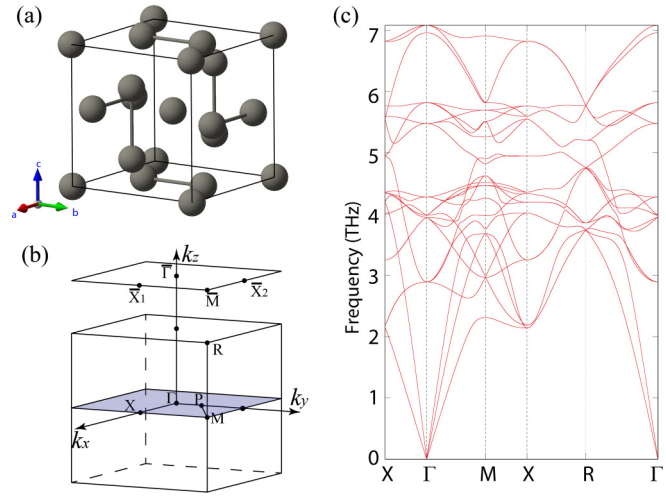

FIG. 1. (a) Crystal structure of β-W. (b) Its first Brillouin (BZ) zone and its (001) surface BZ. In the bulk BZ the shadowed $k_z=0$ plane is a mirror plane and the P-M direction shows a special BZ direction in order to illustrate Dirac cones [here the point P is defined to locate at $(0.00, 0.22, 0.00)\times\frac{2\pi}{a}$]. (c) DFT-derived phonon dispersion at the equilibrium state of the β-W.

B. Electronic structure and its topology

We have studied the electronic structure of β-W without and with the SOC. As shown in Fig. 2(a) for the case without the SOC effect, it can be seen that d-like orbits dominate the Fermi level. In particular, due to the occurrence of the band inversion between $d_{xz}+d_{yz}$ and d_{z^2} at the M point at the BZ boundary there exist four linearly band crossing points around the Fermi level. These four quasilinear band crossing points locate along the X-M and Γ-M directions near the Fermi level. Interestingly, these four crossing points are not isolated and they compose into two circlelike closed loops to form the so-called Dirac nodal lines (DNLs) around the centered M point exactly locating in the $k_z=0$ plane. As shown in Fig. 4(a), these two DNLs (as marked by red) are indeed centered at the M point, with a wavelike shape in energies very close to the Fermi level. To confirm the topological properties of these two DNLs, we have calculated their Berry phases. In a 3D BZ, the berry phase can be defined as

$$\gamma_n=\oint_C \mathbf{A}_n(\mathbf{k})\cdot d\mathbf{l}, \tag{1}$$

where $\mathbf{A}_n(\mathbf{k})=i\langle u_n(\mathbf{k})|\nabla_k|u_n(\mathbf{k})\rangle$ is the Berry connection and $u_n(\mathbf{k})$ is the Bloch wave function of the nth band. Following this expression, we need to define a closed circle centered at a momentum position on the targeted DNL, as illustrated by a black closed circle in Fig. 4(a). However, it needs to be emphasized that the selected radius of the closed circle going around each DNL can be arbitrarily large, as long as it does not cover the other DNL. Importantly, we have found that the Berry phase is $-\pi$ for this defined closed circle, indicating that these DNLs are topologically nontrivial in the β-W phase without the SOC inclusion. In addition, at the energy at about 0.5 eV below the Fermi level, we have indeed observed the other two DNLs also around the centered M point due to the similar band inversion as shown in Fig. 2(a).

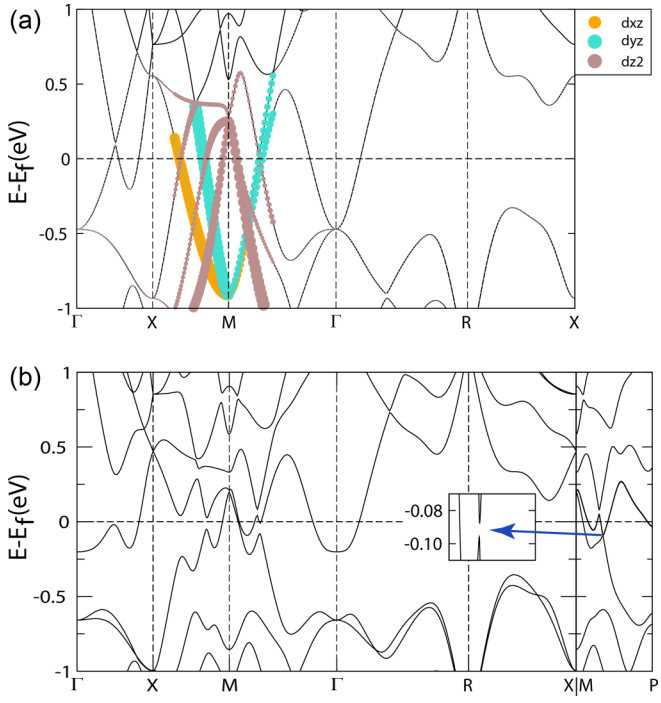

FIG. 2. Electronic band structures along high symmetry lines. (a) Calculated electronic band structures and their components in the absence of spin-orbit coupling (SOC). Different colors represent different d-like orbits and the size of circles denotes the weight of the targeted orbital states. (b) Band structure with the SOC inclusion. The coordinate of point P is $(0.00, 0.22, 0.00)\times\frac{2\pi}{a}$ and one of the massive Dirac bands (MDBs) locates on the M-P line. The inset in (b) shows the tiny band gap of the MDBs.

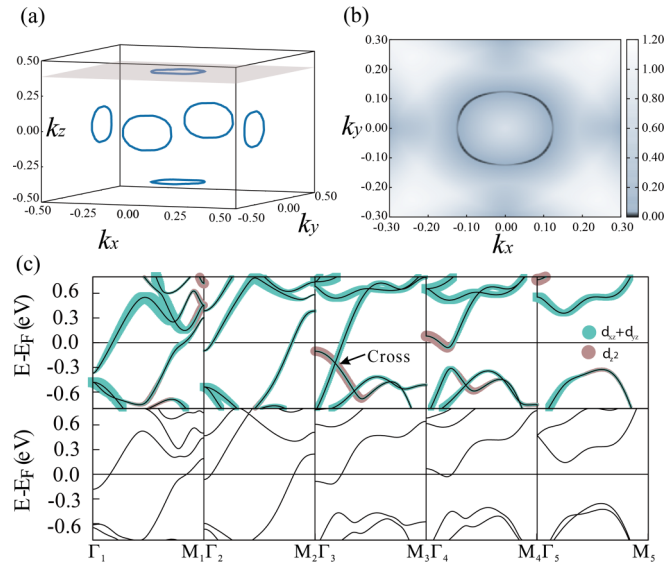

FIG. 3. The out-of-plane Dirac nodal line's distribution and electronic band structures with and without SOC. (a) Without the SOC inclusion, the 3D distribution of DNL in the BZ. (b) The band gap distribution between those two crossing bands on the $k_z = 0.3891$ plane as shaded in (a). Note that in (b) the band gaps are almost zero on the $k_z = 0.3891$ plane but at some points their values are not strictly zero, mainly because this DNL does not strictly locate on this plane and indeed has a wavelike shape fluctuating along k_z direction due to the lack of a mirror plane. (c) The band structures along the defined Γ_i -M_i paths ($i = 1,..., 5$, referring to different k_z values) paralleling to the high-symmetry Γ-M path. Upper panel: Without the SOC inclusion; lower panel: with the SOC inclusion. When the Γ_3-M_3 path ($k_z = 0.3891$) exactly passes through the DNL, there exists a crossing point at $(0.0865, 0.0865, 0.3891)\times\frac{2\pi}{a}$ in the case without the SOC inclusion. However, by switching on the SOC effect, this crossing point opens into a gap in the lower panel of (c).

In particular, we would like to emphasize that the robust stabilities of these DNLs are indeed protected by the band inversion in combination with both time-reversal symmetry and mirror symmetry, in the similarity with what we observed in beryllium [31] and in TiSi [32]. In addition to these above-mentioned DNLs constrained in the mirror planes, we have still observed another typical DNL in the case without the SOC inclusion. As shown in Fig. 3(a), this DNL does not locate on any mirror plane. Due to the crystal symmetry, in the 3D BZ there are six such DNLs. Although this DNL looks like a flat circle as shown in the shaded plane in Fig. 3(a), it is indeed not flat at all. In contrast, this DNL slightly waves along the k_z direction, only occurring in a very tiny k_z scale from $k_z = 0.3886$ to $k_z = 0.3918$ [Fig. 3(b)]. Therefore, we have to adopt a much denser k mesh to sample this DNL. In our current calculations we have hence used the 8 120 601 k points in a very small part of the BZ to identify this DNL. We have analyzed its band inversion, which occurs between the $d_{xz} + d_{yz}$ and d_{z^2} orbitals. Its Berry phase has been also derived to be π, evidencing its topological nontrivial nature.

It is well known that these DNLs can indeed split into various topological insulators, Dirac semimetals and Weyl semimetals upon different atomic masses or broken symmetries. Because the tungsten atom in the β-W phase has a relatively strong SOC effect, its SOC existence definitely lifts up the degeneracy on the DNLs or DPs. For our case β-W, with the SOC inclusion, the inversion symmetry is still present ($\mathcal{P}$) and the time-reversal operator now satisfies $\mathcal{T}^2 = -1$. This fact, $(\mathcal{PT})^2 = -1$, reveals that the two-band Kramers' degeneracy always occurs at every k momentum in the whole BZ. It means that each band is doubly degenerate in both Fig. 2(b) and the lower panel of Fig. 3(c).

Importantly, with the SOC inclusion the calculations have revealed that (i) both the DNL crossed by d_{xz} and d_{z^2} orbitals in Fig. 2 and the DNL crossed by $d_{xz} + d_{yz}$ and d_{z^2} orbitals in Fig. 3 totally split apart now. Taking the DNL as an example in Fig. 3, in the upper panel of Fig. 3(c) without the SOC inclusion the band structures parallel to the high symmetry Γ-M path with increasing k_z exhibits a strict band crossing along the the Γ_3-M_3 path at $k_z = 0.3891$. This crossing point is exact on this DNL. Once the SOC is switched on, this crossing point is clearly witnessed to be open, as shown in the lower panels of Fig. 3(c). (ii) The other DNL crossed by d_{yz} and d_{z^2} orbitals is broken into two classes of new symmetry-inequivalent *massive Dirac bands* (MDBs), locating at $(0.3244, 0.4052, 0.0)\times\frac{2\pi}{a}$ and $(0.4060, 0.3240, 0.0)\times\frac{2\pi}{a}$, respectively.

It is well known that in Dirac semimetals (i.e., Na_3Bi [33–37] and Cd_3As_2 [38]) usually host massless DPs featured by linear band crossings around the Fermi level due to the band inversion protected by various possible symmetries. The

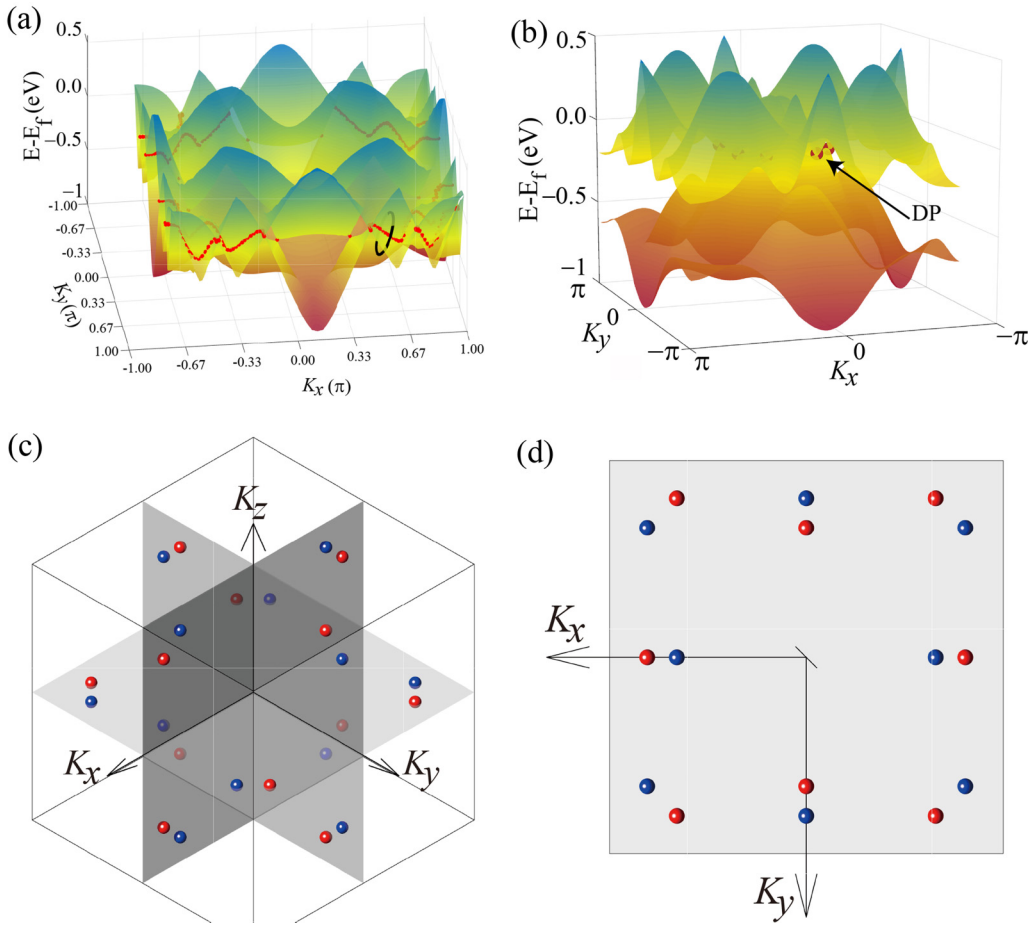

FIG. 4. (a) 3D plot of the electronic band structures of the highest valence band and the lowest conduction band at the $k_z = 0$ plane in the β-W case without the SOC inclusion (the center is the Γ point). The red loops denote the DNLs and the black circle refers to the defined closed path centering at a point of the DNL. (b) 3D plot of the electronic band structures of the highest valence band and the lowest conduction band at the $k_z = 0$ plane in the β-W case with the SOC inclusion (the center is the M point). The red balls denote the MDBs formed by switching SOC on. (c) and (d) The spatial distribution of MDBs in the BZ. Red and blue balls represent two types of symmetric-inequivalent MDBs viewed along the ⟨111⟩ direction and along the top of the ⟨001⟩ direction.

fact means that at the massless DPs the zero band gap with linear band crossing has to exist. However, in difference from massless DPs, in our β-W case the massive Dirac bands (MDBs) imply the quasi-three-dimensional DPs with a tiny mass gap opening of only 7 meV, as illustrated in Fig. 2(b). Recently, the MDBs have been experimentally observed in a ferromagnetic kagome metal of Fe_3Sn_2 [18] and in a magnetically doped topological insulator $Bi_{0.99}Mn_{0.01}Se_3$ [19]. In order to visualize the MDBs in the SOC-containing case of β-W, we have compiled a 3D plot for both the highest valence and the lowest conduction bands on the $k_z = 0$ plane, as illustrated in Fig. 4(b) in which a MDB is clearly shown. In terms of symmetry analysis with the SOC inclusion, each type of MDBs can be symmetrically extended into 12 MDBs in the whole 3D BZ and in total there exist 24 MDBs. It needs to be emphasized that these MDBs in β-W occur neither at any high-symmetry paths nor at any high-symmetry points. This is mainly because the MDBs need no symmetric protections and it is similar to Weyl nodes in Weyl semimetals which can occur at any position. Symmetrically, these MDBs with the SOC inclusion indeed obeys the threefold rotational symmetry along the ⟨111⟩ direction and three mirror symmetries (M_x, M_y, and M_z), as illustrated in Figs. 4(c) and 4(d), respectively. The red and blue balls represent the two types of symmetry-inequivalent MDBs. From Fig. 4(c), in the view along the ⟨111⟩ direction, the MDBs are constrained by the C_{3z} rotational symmetry and in the top view along the ⟨001⟩ direction these MDBs obey mirror symmetries of both M_x and M_y [Fig. 4(d)]. In addition, these MDBs locate at almost the same energy around 87 meV slightly below the Fermi level in Fig. 2(b). In particular, it needs to be emphasized that the occurrence of the MDBs would be highly important to understand the novel large intrinsic spin Hall conductivity found, both experimentally and theoretically, in β-W [10,11,16], because the recent study [18] revealed that the MDBs generate Berry-curvature-induced anomalous Hall conductivity in Fe_3Sn_2.

C. Nontrivial topological surface states

As already observed in the typical 3D Dirac semimetals (i.e., Na_3Bi [33–37] and Weyl semimetals [39–41]), they will exhibit the nontrivial surface Fermi arcs. On the surfaces of β-W phase, many topologically nontrivial surface states can

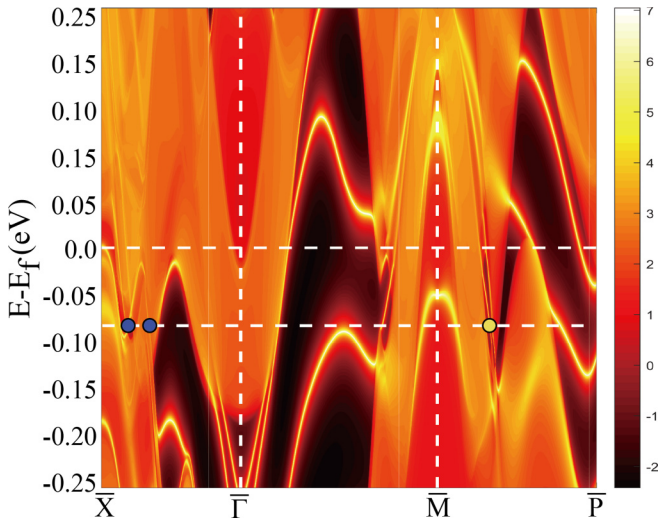

FIG. 5. Electronic band of the (001) surface of β-W. The yellow solid circles represent the single MDBs and the blue solid circles are the projected double MDBs. The zero energy refers to the Fermi level and the MDBs locate at the energy of 87 meV below the Fermi level.

be expected due to the occurrence of 24 MDBs in its bulk phase [see Figs. 4(c) and 4(d)]. To illustrate these features, we have plot the (001) surface electronic band structure in Fig. 5 along the high-symmetry $\overline{X} \to \overline{\Gamma} \to \overline{M} \to \overline{P}$ directions. It can be seen that those stronger intensities as marked by brilliant yellow correspond to the localized surface states, whereas the shadow bands in the background reflect well the surface projection of the bulk electronic bands. To be specific, at the energy of 87 meV below the Fermi level the quasi-Dirac-like crossing points can be observed along both the $\overline{X} \to \overline{\Gamma}$ (as marked by blue circles) and the $\overline{M} \to \overline{P}$ directions (as marked by yellow circles). They are the projections of the bulk MDBs on the (001) surface. In particular, it needs to be emphasized that the blue circles denote the projection of two MDBs onto the same position (double MDBs), whereas the yellow circle is the projection of single MDB in the BZ along the $\langle 001 \rangle$ direction.

Based on the symmetry analysis, the (001) surface remains unchanged under the C_2 rotational symmetry or two mirror symmetries [i.e., $C_2 : (x, y, z) \to (-x, -y, z)$, $M_x : (x, y, z) \to (-x, y, z)$, and $M_y : (x, y, z) \to (x, -y, z)$]. The MDBs on the k_x and k_y axes are the overlapped projections of two MDBs, while the MDBs on the generic momentum are the projection of a single MDB. Physically it can be understandable that each DP can be treated as the overlapping of two Weyl nodes with opposite chiral charges. The nontrivial surface Fermi arcs can be expected to connect two Weyl nodes with opposite topological charges. As a result, on the surface

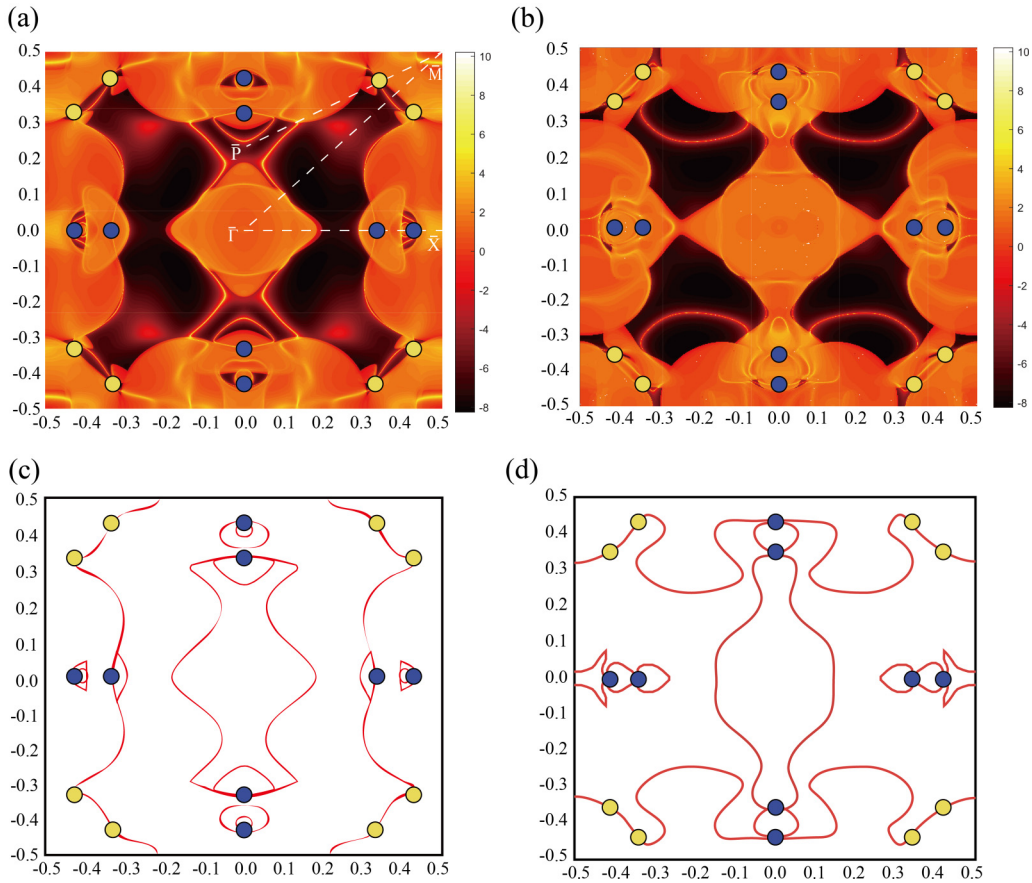

FIG. 6. Fermi surfaces and surface states of the (001) surface of β-W. The yellow solid circles represent the single MDBs and the blue solid circles are the projected double MDBs. (a) The Fermi arcs and MDBs on the surface at a constant energy (87 meV) below the Fermi level. (c) The corresponding illustrations of the nontrivial Fermi arcs connecting MDBs in (a). (b) The Fermi arcs and MDBs on the surface at the Fermi level. (d) The corresponding illustrations of the nontrivial Fermi arcs connecting MDBs in (b).

single DP always connects two Fermi arcs and the double overlapped DPs should connect four Fermi arcs. Interestingly, for MDBs we have also observed the similar connections of nontrivial Fermi arcs. To illustrate these features, we have compiled the (001) Fermi surface at the energy of 87 meV below the Fermi level in Fig. 6(a) and at the Fermi level in Fig. 6(b). In agreement with above analysis, on the (001) Fermi surface the double MDBs and single MDBs exist. Along the defined $\overline{M} \rightarrow \overline{P}$ path there exists a single MDB around the $\overline{M}$ point [Fig. 6(a)], which is the projection of the single MDB in the bulk BZ. According to the symmetric operation, in total there are eight such single MDBs on the (001) Fermi surface. In addition, we have observed double MDBs along the high-symmetry $\overline{\Gamma} \rightarrow \overline{X}$ path in the (001) surface BZ [Fig. 6(a)], which are the overlapped projections of the two MDBs in the bulk BZ. It can be seen that on the (001) surface the topologically nontrivial surface electronic states heavily overlap with the projections of the bulk electronic bands. But, some topologically nontrivial surface arclike states can be observed. We have thus figured out the arc connections among these MDBs in Fig. 6(c) from which all single MDBs connect two arcs and all double MDBs connect four arcs can be seen. Furthermore, we have also derived the Fermi surface at the Fermi energy in Fig. 6(b). It can be seen that increasing the chemical potential significantly influences the patterns of the Fermi arcs. Some topological surface nontrivial arclike states are clearly originated from the MDBs, which can be viewed in our sketch connections in Fig. 6(d). Besides these nontrivial surface arc states, we also see some trivial surface states around the $\overline{M}$ point in the corner of the BZ mainly due to the truncation of the surface wave functions.

Finally, we would like to emphasize that in some early studies β-W films were confirmed to exhibit superconductivity with the critical transition temperature T_c of 2–3.5 K [42–44]. This value is two orders of magnitude higher than that of bulk α-W. Importantly, the enhanced superconductivity of β-W films was interpreted to be Ginzburg's surface-state superconductivity [45]. It would be highly interesting to investigate the effect of the nontrivial surface states of topological Dirac metal of β-W on its superconductivity.

IV. CONCLUSION

By means of first-principles calculations, we focused on the topological electronic structures of β-tungsten with space group $Pm\bar{3}n$, revealing that it is a topological massive Dirac metal which hosts 24 robust MDBs in its bulk phase with SOC inclusion. We investigated the band inversions and Berry phases of the DNL, confirming the nontrivial topological nature of β-W. The nontrivial surface states have also been analyzed and all the MDBs are connected by fermi arcs.

ACKNOWLEDGMENTS

Work was supported by the National Science Fund for Distinguished Young Scholars (Grant No. 51725103) and by the National Natural Science Foundation of China (Grants No. 51671193 and No. 51474202). All calculations have been performed on the high-performance computational cluster in the Shenyang National University Science and Technology Park.

J.L. and S.U. contributed equally to this work.

[1] W. P. Davey, The lattice parameter and density of pure tungsten, Phys. Rev. **26**, 736 (1925).

[2] D. Choi, K. Barmak, A. Darbal, X. Liu, A. Warren, and K. R. Coffey, Phase, grain structure, stress, and resistivity of sputter-deposited tungsten films, J. Vac. Sci. Technol. A **29**, 051512 (2011).

[3] D. Choi, C.-S. Kim, S. Chung, A. P. Warren, N. T. Nuhfer, M. F. Toney, K. R. Coffey, and K. Barmak, Electron mean free path of tungsten and the electrical resistivity of epitaxial (110) tungsten films, Phys. Rev. B **86**, 045432 (2012).

[4] K. Barmak, J. Liu, L. Harlan, P. Xiao, J. Duncan, and G. Henkelman, Transformation of topologically close-packed β-W to body-centered cubic α-W: Comparison of experiments and computations, J. Chem. Phys. **147**, 152709 (2017).

[5] H. T. Lee, A. A. Haasz, J. W. Davis, and R. G. Macaulay-Newcombe, Hydrogen and helium trapping in tungsten under single and sequential irradiations, J. Nucl. Mater **360**, 196 (2007).

[6] S. Manipatruni, D. E. Nikonov, and A. Young, Energy-delay performance of giant spin Hall effect switching for dense magnetic memory, Appl. Phys. Express **7**, 103001 (2014).

[7] D. Choi, M. Moneck, X. Liu, S. J. Oh, C. R. Kagan, K. R. Coffey, and K. Barmak, Crystallographic anisotropy of the resistivity size effect in single crystal tungsten nanowires, Sci. Rep. **3**, 2591 (2013).

[8] P. N. Dyachenko, S. Molesky, A. Y. Petrov, M. Störmer, T. Krekeler, S. Lang, M. Ritter, Z. Jacob, and M. Eich, Controlling thermal emission with refractory epsilon-near-zero metamaterials via topological transitions, Nat. Commun. **7**, 11809 (2016).

[9] S. Javadi, B. Ouyang, Z. Zhang, M. Ghoranneviss, A. S. Elahi, and R. S. Rawat, Effects of fusion relevant transient energetic radiation, plasma and thermal load on PLANSEE double forged tungsten samples in a low-energy plasma focus device, Appl. Surf. Sci. **443**, 311 (2018).

[10] C. F. Pai, L. Liu, Y. Li, H. W. Tseng, D. C. Ralph, and R. A. Buhrman, Spin transfer torque devices utilizing the giant spin Hall effect of tungsten, Appl. Phys. Lett. **101**, 122404 (2012).

[11] X. L. Sui, C. Wang, J. Kim, J. Wang, S. H. Rhim, W. H. Duan, and N. Kioussis, Giant enhancement of the intrinsic spin Hall conductivity in β-tungsten via substitutional doping, Phys. Rev. B **96**, 241105(R) (2017).

[12] M. Costa, A. T. Costa, R. Q. Wu, and R. B. Muni, β-tungsten: A promising metal for spintronics, J. Phys. Condens. Matter **30**, 305802 (2018).

[13] I. M. Miron, K. Garello, G. Gaudin, P.-J. Zermatten, M. V. Costache, S. Auffret, S. Bandiera, B. Rodmacq, A. Schuhl, and P. Gambardella, Perpendicular switching of a single ferromagnetic layer induced by in-plane current injection, Nature (London) **476**, 189 (2011).

[14] L. Liu, T. Moriyama, D. C. Ralph, and R. A. Buhrman, Spin-Torque Ferromagnetic Resonance Induced by the Spin Hall Effect, Phys. Rev. Lett. **106**, 036601 (2011).

[15] L. Liu, C.-F. Pai, Y. Li, H. W. Tseng, D. C. Ralph, and R. A. Buhrman, Spin-torque switching with the giant spin Hall effect of tantalum, Science **336**, 555 (2012).

[16] Q. Hao, and G. Xiao, Giant Spin Hall Effect and Switching Induced by Spin-Transfer Torque in a $W/Co_40Fe_40B_20/MgO$ Structure with Perpendicular Magnetic Anisotropy, Phys. Rev. Appl. **3**, 034009 (2015).

[17] A. R. Mellnik, J. S. Lee, A. Richardella, J. L. Grab, P. J. Mintun, M. H. Fischer, A. Vaezi, A. Manchon, E. A. Kim, N. Samarth, and D. C. Ralph, Spin-transfer torque generated by a topological insulator, Nature (London) **511**, 449 (2014).

[18] L. Ye, M. Kang, J. Liu, F. V. Cube, C. R. Wicker, T. Suzuki, C. Jozwiak, A. Bostwick, E. Rotenberg, D. C. Bell, L. Fu, R. Comin, and J. G. Checkelsky, Massive Dirac fermions in a ferromagnetic kagome metal, Nature (London) **555**, 638 (2018).

[19] Y. L. Chen, J.-H. Chu, J. G. Analytis, Z. K. Liu, K. Igarashi, H.-H. Kuo, X. L. Qi, S. K. Mo, R. G. Moore, D. H. Lu, M. Hashimoto, T. Sasagawa, S. C. Zhang, I. R. Fisher, Z. Hussain, and Z. X. Shen, Massive Dirac fermion on the surface of a magnetically doped topological insulator, Science **329**, 659 (2010).

[20] P. Hohenberg and W. Kohn, Inhomogeneous electron gas, Phys. Rev. **136**, B864 (1964).

[21] W. Kohn and L. J. Sham, Self-consistent equations including exchange and correlation effects, Phys. Rev. **140**, A1133 (1965).

[22] G. Kresse and J. Hafner, *Ab initio* molecular dynamics for liquid metals, Phys. Rev. B **47**, 558 (1993).

[23] G. Kresse and J. Furthmüller, Efficiency of ab-initio total energy calculations for metals and semiconductors using a plane-wave basis set, Comput. Mater. Sci. **6**, 15 (1996).

[24] P. E. Blöchl, Projector augmented-wave method, Phys. Rev. B **50**, 17953 (1994).

[25] J. P. Perdew, K. Burke, and M. Ernzerhof, Generalized Gradient Approximation Made Simple, Phys. Rev. Lett. **77**, 3865 (1996).

[26] S. Baroni, S. Gironcoli, A. D. Corso, and P. Giannozzi, Phonons and related crystal properties from density-functional perturbation theory, Rev. Mod. Phys. **73**, 515 (2001).

[27] A. Togo, F. Oba, and I. Tanaka, First-principles calculations of the ferroelastic transition between rutile-type and $CaCl_2$-type SiO_2 at high pressures, Phys. Rev. B **78**, 134106 (2008).

[28] M. P. Lopez Sancho, J. M. Lopez Sancho, J. M. L. Sancho, and J. Rubio, Highly convergent schemes for the calculation of bulk and surface Green functions, J. Phys. F: Metal Phys. **15**, 851 (1985).

[29] A. J. Narasimham, M. Medikonda, A. Matsubayashi, P. Khare, H. Chong, R. J. Matyi, A. Diebold, and V. P. Labella, Fabrication of 5–20 nm thick β-W films, AIP Adv. **4**, 117139 (2014).

[30] W. R. Morcom, W. L. Worrell, H. G. Sell, H. I. Kaplan, Preparation and characterization of beta-tungsten, a metastable tungsten phase, Metal. Trans. **5**, 155 (1974).

[31] R. H. Li, H. Ma, X. Y. Cheng, S. L. Wang, D. Z. Li, Z. Y. Zhang, Y. Y. Li, and X.-Q. Chen, Dirac Node Lines in Pure Alkali Earth Metals, Phys. Rev. Lett. **117**, 096401 (2016).

[32] J. X. Li ,H. Ma, Q. Xie, S. B. Feng, S. Ullah, R. H. Li, J. H. Dong, D. Z. Li, Y. Y. Li, and X.-Q. Chen, Topological quantum catalyst: Dirac nodal line states and a potential electrocatalyst of hydrogen evolution in the TiSi family, Sci. China Mater. **61**, 23 (2018).

[33] Z. J. Wang, Y. Sun, X.-Q. Chen, C. Franchini, G. Xu, H. M. Weng, X. Dai, and Z. Fang, Dirac semimetal and topological phase transitions in A_3Bi (A=Na, K, Rb), Phys. Rev. B **85**, 195320 (2012).

[34] Z. K. Liu, B. Zhou, Y. Zhang, Z. J. Wang, H. M. Weng, D. Prabhakaran, S.-K. Mo, Z. X. Shen, Z. Fang, X. Dai, Z. Hussain, and Y. L. Chen, Discovery of a three-dimensional topological Dirac semimetal, Na_3Bi, Science **343**, 864 (2014).

[35] X. Y. Cheng, R. H. Li, Y. Sun, X.-Q. Chen, D. Z. Li, and Y. Y. Li, Ground-state phase in the three-dimensional topological Dirac semimetal Na_3Bi, Phys. Rev. B **89**, 245201 (2014).

[36] X. Y. Cheng, R. H. Li, D. Z. Li, Y. Y. Li, and X.-Q. Chen, Combined fast reversible liquidlike elastic deformation with topological phase transition in Na_3Bi, Phys. Rev. B **92**, 155109 (2015).

[37] S.-Y. Xu, C. Liu, S. K. Kushwaha, R. Sankar, J. W. Krizan, I. Belopolski, M. Neupane, G. Bian, N. Alidoust, T. R. Chang, H. T. Jeng, C. Y. Huang, W. F. Tsai, H. Lin, P. P. Shibayev, F. C. Chou, R. J. Cava, and M. Z. Hasan, Observation of Fermi arc surface states in a topological metal, Science **347**, 294 (2015).

[38] Z. J. Wang, H. M. Weng, Q. S. Wu, X. Dai, and Z. Fang, Three-dimensional Dirac semimetal and quantum transport in Cd_3As_2, Phys. Rev. B **88**, 125427 (2013).

[39] X. Wan, A. M. Turner, A. Vishwanath, and S. Y. Savrasov, Topological semimetal and Fermi-arc surface states in the electronic structure of pyrochlore iridates, Phys. Rev. B **83**, 205101 (2011).

[40] H. M. Weng, C. Fang, Z. Fang, B. A. Bernevig, and X. Dai, Weyl Semimetal Phase in Noncentrosymmetric Transition-Metal Monophosphides, Phys. Rev. X **5**, 011029 (2015).

[41] S. M. Huang, S. Y. Xu, I. Belopolski, C. C. Lee, G. Q. Chang, B. K. Wang, N. Alidoust, G. Bian, M. Neupane, C. L. Zhang, S. Jia, A. Bansil, H. Lin, and M. Z. Hasan, A Weyl Fermion semimetal with surface Fermi arcs in the transition metal monopnictide TaAs class, Nat. Commun. **6**, 7373 (2015).

[42] W. L. Bond, A. S. Cooper, K. Andres, G. W. Hull, T. H. Geballe, and B. T. Matthias, Superconductivity in Films of β Tungsten and Other Transition Metals, Phys. Rev. Lett. **15**, 260 (1965).

[43] R. Rosenbaum, M. Ben-Shlomo, and S. Goldsmith, Low-temperature electronic transport properties of W, Mo, Ta, and Zr thin films, Phys. Rev. B **39**, 10009 (1989).

[44] M. Strongin, O. F. Kammerer, and A. Paskin, Superconducting Transition Temperature of Thin Films, Phys. Rev. Lett. **14**, 949 (1965).

[45] V. L. Ginzburg, On Surface Superconductivity, Phys. Lett. **13**, 101 (1964).